Materials Advances

ROYAL SOCIETY OF CHEMISTRY

PAPER

View Article Online
View Journal | View Issue

Cite this: *Mater. Adv.*, 2024, 5, 1217

Received 25th October 2023,
Accepted 19th December 2023

DOI: 10.1039/d3ma00903c

rsc.li/materials-advances

Advancing very high temperature thermoelectric performance of Yb_4Sb_3 through dual-substitutions: a combined experimental and theoretical study

Hugo Bouteiller, *[ab] Vincent Pelletier, [c] Sylvain Le Tonquesse, [ab]
Bruno Fontaine,[cd] Takao Mori, [ef] Jean-François Halet, [bc] Régis Gautier, *[c]
David Berthebaud *[bg] and Franck Gascoin [a]

This article reports and discusses the synthesis and the transport properties of the binary rare-earth antimonide Yb_4Sb_3 and some of its substituted derivatives. Specifically, co-substitution of La on the Yb site and Bi on the Sb site was attempted to further improve its thermoelectric properties. The solubility limit of the $La_xYb_{4-x}Sb_{2.8}Bi_{0.2}$ solid solution was established to be x = 0.3. Subsequent synthesis of x = 0.1, 0.2, and 0.3 compositions at a larger scale enabled their transport property evaluation and the comparison with Yb_4Sb_3. The Seebeck coefficient of the substituted compounds was found to be similar to the pristine material from 373 to 1273 K, while an increase in resistivity was observed. Detailed DFT calculations confirmed that the Seebeck coefficient may not be significantly improved by La substitutions and explained the p-type conducting behavior at high temperatures of the title compounds. The thermal conductivity of $La_{0.2}Yb_{3.8}Sb_{2.8}Bi_{0.2}$ was found to be reduced by about 30% compared to that of the binary Yb_4Sb_3. The figure of merit zT of the parent Yb_4Sb_3 compound reaches 0.5 at 1273 K. While dual substitutions have not permitted a significant improvement in the figure of merit mostly due to a resistivity increase, this study provides a stepping stone for further optimization.

Introduction

In response to the escalating global demand for energy, effective utilization of waste heat through thermoelectric energy conversion has garnered substantial attention.[1–3] Industries such as steel mills or power plants operating at very high temperatures, typically above 800 K, dissipate significant amounts of heat that could be converted into electricity by thermoelectric generators.[4,5] The conversion efficiency of such modules mostly depends on the performance of the integrated thermoelectric components, which is evaluated by the adimensional figure of merit $zT = S^2T/(\rho\kappa)$, S being the Seebeck coefficient, T the absolute temperature, ρ the resistivity and κ the thermal conductivity of the material, respectively. Currently, viable solutions within the realm of very high temperatures remain rather constrained, owing to the scarcity of materials presenting suitable transport properties above 800 K.[6–9] Both n- and p-type SiGe have been used for decades as the main solution by NASA,[10] especially for radio-isotope thermoelectric generators (RTGs),[11] complemented by the Zintl phase $Yb_{14}MnSb_{11}$ which serves as a p-type alternative.[12] Recent investigations have highlighted the potential candidacy of $Yb_{21}Mn_4Sb_{18}$ as well within this temperature range, exhibiting a zT value of 0.8 at 800 K.[13] Furthermore, Half-Heusler compounds have also emerged as promising candidates for the development of high temperature thermoelectric modules up to 1100 K.[14] While the fabrication of thermoelectric devices for power generation necessitates meticulous considerations encompassing low contact resistances and harmonious thermal expansion,[15] the paramount factor governing net power generation indisputably remains the figure of merit exhibited by both n-type and p-type constituents.[16] Therefore, the pursue of novel materials showcasing optimal transport properties in the very high temperature range (800–1300 K) is much needed and stand as the focus of this work.

---

[a] Laboratoire CRISMAT, ENSICAEN, UNICAEN, CNRS Normandie Univ. (UMR 6508), Caen, France
[b] CNRS–Saint-Gobain–NIMS, IRL 3629, Laboratory for Innovative Key Materials and Structures (LINK), National Institute for Materials Science (NIMS), 305–0044, Tsukuba, Japan
[c] Univ Rennes, CNRS, Ecole Nationale Supérieure de Chimie de Rennes, ISCR-UMR6226, F–35000, Rennes, France
[d] Saint-Cyr Coëtquidan Military Academy, CReC, F–56380, Guer, France
[e] Graduate School of Pure and Applied Sciences, University of Tsukuba, 305–8671, Tsukuba, Japan
[f] National Institute for Materials Science (NIMS), WPI-MANA, University of Tsukuba, 305–0044, Tsukuba, Japan
[g] Nantes Université, CNRS, Institut des Matériaux de Nantes Jean Rouxel, IMN, Nantes F–44000, France

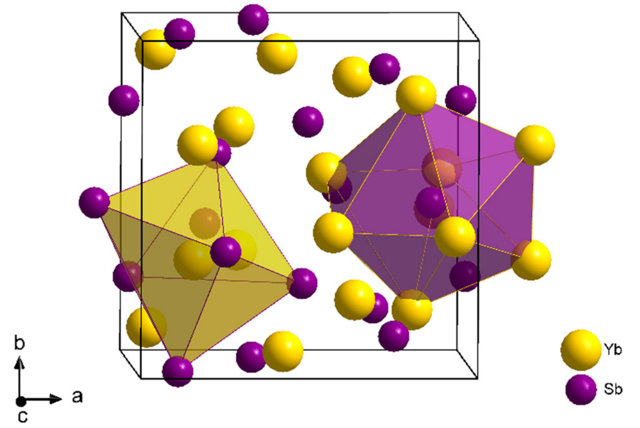

Fig. 1 Crystal structure of Yb_4Sb_3 and coordination polyhedra of Yb (yellow) and Sb (purple) atoms.

$La_{3-x}Te_4$ is a promising n-type material that exhibits a zT above unity around 1300 K.[17] This compound crystallizes in the Th_3P_4 structure type, wherein vacancies are accommodated on the rare-earth sites. Rare-earth antimonides of typical formula RE_4Sb_3 (RE = Yb, La, Sm, Ce) are presenting the anti-Th_3P_4 crystal structure.[18] In this cubic structural arrangement (space group $I\bar{4}3d$), rare-earth atoms occupy P sites (Wyckoff position 16c) at the center of a distorted octahedron, while antimony atoms occupy Th sites (12a), forming a bis-disphenoid environment shaped by two interpenetrated Yb tetrahedra (Fig. 1). As it turns out, La_4Sb_3, Sm_4Sb_3 and Ce_4Sb_3 all exhibit n-type metallic conductive behavior with low Seebeck values in the 300–1300 K temperature range.[19] Yb_4Sb_3, on the other hand, present a quite different behavior: while the Seebeck coefficient is negative at room temperature (around -20 μV K^{-1}), it then increases linearly with temperature, reaching 70 μV K^{-1} at 1300 K according to previous studies.[19,20] Meanwhile, the resistivity remain consistently low, as expected for metallic conductive behavior, with values of about 1.2 mΩ cm at 1300 K,[20] leading to a decent power factor around 4 μW cm^{-1} K^{-2} at this temperature.[21] For this reason, Yb_4Sb_3 was investigated for possible thermoelectric applications at very high temperature as a p-type counterpart of n-type $La_{3-x}Te_4$. An intriguing aspect of Yb_4Sb_3 is its p-type conduction, dominated by hole carriers above 600 K. This is notable since other rare-earth antimonides consistently exhibit n-type behavior across all temperatures. This peculiarity arises from Yb's mixed valency, switching between 2+ and 3+ oxidation states. However, magnetic studies have shown that the oxidation state of Yb atoms was predominantly 2+, not 3+.[19] This suggests, based on the Zintl formalism, that Yb atoms donate only 8 electrons per formula unit to the anionic framework, which is comprised of Sb atoms able to accept 9 electrons overall per formula unit. This electron deficiency might explain the p-type conductive behavior in Yb_4Sb_3 above 600 K, but this needs to be confirmed by further theoretical investigations.

Efforts to enhance transport properties have been pursued through various strategies. Initially, substituting La for Yb was explored to lower the concentration of charge carriers, specifically holes, present in Yb_4Sb_3 at high temperatures. This exchange of $Yb^{2+/3+}$ atoms with La^{3+} atoms aimed to enhance the Seebeck coefficient through the reduction of available holes. Several compositions were investigated and it was shown that $La_{0.5}Yb_{3.5}Sb_3$ exhibited the best performance with an improvement of the power factor up to 10 μW cm^{-1} K^{-2} at 1300 K.[19] Associated to a significantly reduced thermal conductivity of 1.7 W m^{-1} K^{-1} at 1300 K, $La_{0.5}Yb_{3.5}Sb_3$ displayed a promising zT value of 0.75.[19] Furthermore, substituting a small amount of Sb by Bi also yield positive results. The $Yb_4Sb_{2.8}Bi_{0.2}$ composition, for instance, shows an enhanced power factor of approximately 8 μW cm^{-1} K^{-2} at 1300 K.[20]

Building upon prior research efforts, the main objective of this study was to investigate the outcomes of a dual substitution, involving the replacement of both La on Yb sites and Bi on Sb sites. The aim was to potentially harness synergetic effects in order to further enhance the thermoelectric properties of the parent material. The Bi substitution level was set at $y = 0.2$, guided by the promising outcomes observed for the $Yb_4Sb_{2.8}Bi_{0.2}$ composition's transport properties. Very recently, we used a similar strategy with partial Bi substitution on Sb sites while a partial amount of Yb atoms were replaced by Ce atoms.[22] Findings from this study demonstrated a significant enhancement in the thermoelectric properties of the Ce-substituted solid solution, motivating further exploration into the transport properties of the La-substituted solid solution.

To explore the limits of solubility within the $La_xYb_{4-x}Sb_{2.8}Bi_{0.2}$ solid solution, the La substitution level was progressively increased from $x = 0.1$ to 1. Notably, the replacement of Sb with the larger-radius Bi may allow a broader solubility range in regard to the substitution of La for Yb, eventually leading to a reduction in charge carrier concentration by introducing a greater amount of La into the structure. Upon establishing the solubility limit, the synthesis and preparation of homogeneous $La_xYb_{4-x}Sb_{2.8}Bi_{0.2}$ compositions were undertaken to characterize their transport properties. Additionally, a theoretical analysis was conducted to explore the influence of both La and Bi substitution on the electronic structure of Yb_4Sb_3 and better understand the transport properties of the solid solution. We thus report in this article an unprecedented combined experimental and theoretical investigation on this chemical system which shows great promise for thermoelectric applications in the very high temperature range.

Experimental and theoretical procedures

Synthesis and preparation

Yb_4Sb_3 and substituted $La_xYb_{4-x}Sb_{3-y}Bi_y$ compounds were synthesized in niobium tubes by mixing appropriate amounts of La (ingot, 99.8%), Yb (ingot, 99.8%), Sb (shots, 99.99%) and Bi (shots, 99.999%) within an Ar-filled glovebox. To ensure an inert reaction environment, the niobium tubes were hermetically sealed under high-purity argon, using a custom arc furnace setup, before being enclosed in fused silica tubes and further sealed to prevent oxidation of the niobium containers. The solid solution study was carried out using low quantities of reactants (500 mg).

These samples were heated at 1000 °C during 96 h with heating and cooling ramps of 16 h. Subsequently, Nb containers were opened under argon atmosphere, powders were finely ground, sealed back in new Nb capsules and annealed at 1000 °C for three weeks. Samples aimed at the measurement of the transport properties were shaped from a higher quantity of powder (5 g), heated at 1050 °C, over an 8-day dwell period featuring 10-hour ramps, followed by an annealing at 1000 °C for another 8 days. X-ray diffraction measurements were carried out using an X'Pert Pro MRD (Panalytical) (Cu-Kα1 and Cu-Kα2 radiations) and a D8 Advance Vario1 (Bruker) apparatus (Cu-Kα1 radiation $\lambda = 1.540598$ Å). Structure refinements were performed using the Fullprof suite.[23] Samples were densified by Spark Plasma Sintering using Dr Sinter Lab Jr's SPS-322Lx with ∅10 mm graphite dies. Uniaxial pressure of 50 MPa was applied with a temperature dwell of 1200 °C kept for 10 minutes during a one-hour run, yielding pellets of relative densities beyond 95%. Densified samples were annealed in either Ta or Mo foils at 1000 °C for 24 hours to ensure chemical stability and homogeneity. Composition and microstructure were assessed by scanning electron microscopy coupled with energy-dispersive X-ray spectroscopy. Seebeck coefficient and resistivity were measured from 373 to 1273 K on 3 × 3 × 10 mm samples by a ZEM5 apparatus (ULVAC) and thermal conductivity measurements were performed with a LFA467 HT HyperFlash (Netzsch) under N_2 flux, employing Ø10 mm graphite-coated cylinders of up to 2 mm thickness.

Calculations

All density functional theory (DFT) calculations were performed using the VASP software version 6.2.0.[24–26] and the Perdew, Burke and Ernzerhof (PBE) exchange–correlation functional.[27] Structural optimizations and average properties were performed with a cut-off energy of 350 eV and a 7 × 7 × 7 *k*-points grid sampled by the Monkhorst–Pack method.[28] The band structure was computed with the same cut-off energy using 15 *k*-points per symmetry line.

Electronic transport coefficients were calculated within the Boltzmann Transport Equation. A constant relaxation time τ for the electrons was assumed as well as a rigid band structure,[29,30] as implemented in the BoltzTrap2 code.[31] A 11 × 11 × 11 *k*-point grid was used to compute the band derivatives for transport calculations.

Results and discussion

Synthesis of the binary Yb_4Sb_3 compound

The pristine compound Yb_4Sb_3 was first synthesized. The obtained powder X-ray diffraction pattern was refined by the Le Bail method ($R_p = 2.78$; $R_{wp} = 3.88$), yielding a cell parameter $a = 9.3324(1)$ Å (Fig. 2), which closely aligns with other previously reported values.[18] Very low intensity reflections of Yb_2O_3 were also indexed and attributed to the slightly oxidized Yb starting reagent. Subsequently, partial substitutions of La for Yb and Bi for Sb were carried out.

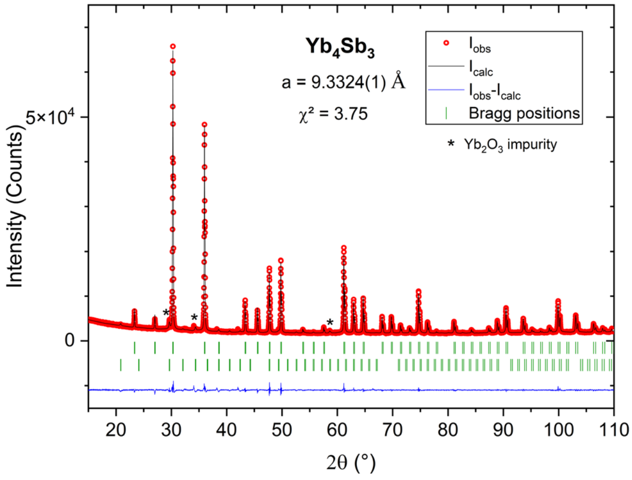

Fig. 2 Le Bail refinement of the X-ray diffraction pattern of Yb_4Sb_3 synthesized in niobium containers. Low intensity peaks could be indexed as Yb_2O_3 impurity. The experimental data are plotted in red symbols, the calculated pattern is drawn with a black line, the difference with a blue line, and the Bragg positions with green vertical ticks.

Study of the $La_xYb_{4-x}Sb_{2.8}Bi_{0.2}$ solid solution

Investigation of the $La_xYb_{4-x}Sb_{2.8}Bi_{0.2}$ solid solution was initiated primarily to identify single-phase compounds for subsequent transport property measurements. Based on the findings from the previously explored $La_xYb_{4-x}Sb_3$ solid solution, where the solubility limit was determined to be $x = 0.5$,[19] it was of interest to investigate the potential influence of partial Sb substitution with the larger-radius Bi atoms. Given the larger atomic radius of Bi (1.60 Å) compared with that of Sb (1.45 Å), the conjecture was that this substitution could open up greater possibilities for La atom substitution on the Yb site. To test this hypothesis, the quantity of La was varied from $x = 0$ to 1, while maintaining a Bi stoichiometry of 0.2 on the Sb site, in line with prior studies.[20,21]

The results sketched in Fig. 3 indicate that starting from the nominal composition $La_{0.6}Yb_{3.4}Sb_{2.8}Bi_{0.2}$, the presence of LaSb is detected in the bulk. This is due to the pronounced incorporation of La, resulting in a biphasic domain under the specific synthesis temperature and pressure conditions. This assumption is supported by the correlation which is observed: higher La amount corresponds to an elevated intensity of LaSb reflections (Fig. 3). In the case of $La_{0.4}Yb_{3.6}Sb_{2.8}Bi_{0.2}$, despite the absence of the LaSb phase, some reflections exhibit distortion, implying that the substitution level is still somewhat excessive, hindering complete integration of La and Bi atoms within the parent structure. However, compositions with $x \leq 0.3$ display no LaSb impurities and exhibit undistorted peaks, signifying successful substitution of La and Bi for Yb and Sb, respectively, in the structure. This solubility limit is slightly lower than that observed in the Ce-inserted $Ce_xYb_{4-x}Sb_{2.8}Bi_{0.2}$ solid solution ($x = 0.5$),[22] mainly owing to the higher atomic radius of La atoms (1.95 Å) compared with Ce atoms (1.85 Å). The refined cell parameters are displayed in Fig. 4. Based on this investigation, compositions with $x = 0.1$, 0.2, and 0.3 have been selected for further synthesis at larger scales, targeting subsequent transport property measurements.

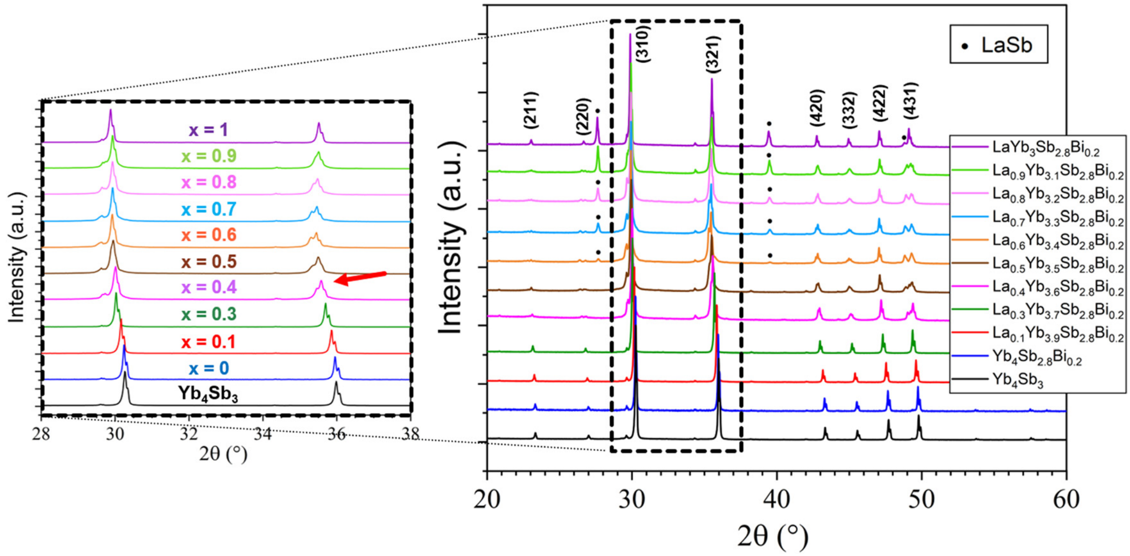

Fig. 3 X-Ray diffraction patterns of Yb_4Sb_3 and the solid solution $La_xYb_{4-x}Sb_{2.8}Bi_{0.2}$ ($0 \leq x \leq 1$). The solubility limit occurs for $x = 0.3$ as diffraction peaks are significantly distorted for higher La substitution. LaSb impurity is observed for $x \geq 0.6$.

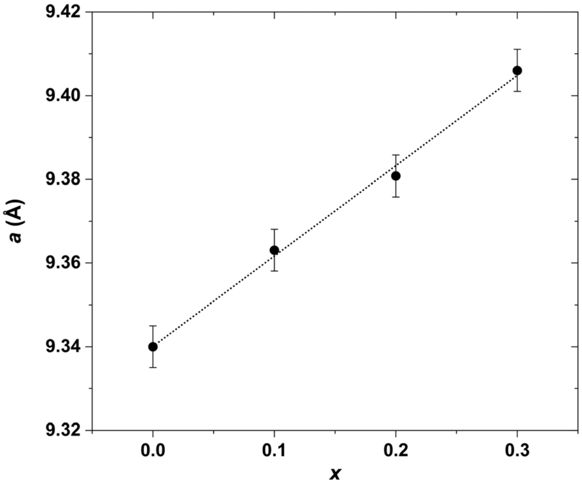

Fig. 4 Cell parameter a of the $La_xYb_{4-x}Sb_{2.8}Bi_{0.2}$ *versus* amount of La (x = 0.1, 0.2 and 0.3) solid solution refined by the Le Bail refinement method. The cell parameter increases linearly with La content, following a classical Vegard law.

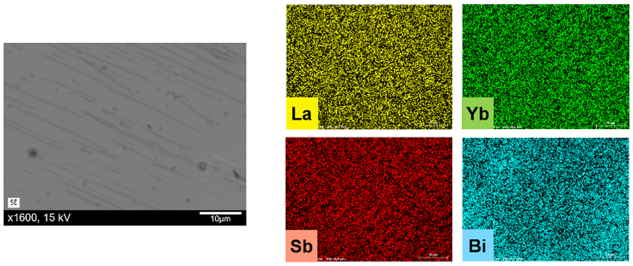

Fig. 5 Electron Dispersive X-ray Spectroscopy characterization of the $La_{0.3}Yb_{3.7}Sb_{2.8}Bi_{0.2}$ compound. The presence of all elements was confirmed with a good homogeneity.

Scanning electron microscopy

Samples of Yb_4Sb_3 and $La_xYb_{4-x}Sb_{2.8}Bi_{0.2}$ (x = 0.1, 0.2 and 0.3) were characterized by SEM on densified samples. Homogeneous densified materials were observed, the illustrative case for x = 0.3 composition being displayed in Fig. 5. The examination of sample surfaces in secondary electrons mode revealed minimal porosity, the slight contrast observed being attributed to the polishing step of the assessed sample. Energy-dispersive spectroscopy analyses confirmed these findings and show great compositional homogeneity, consistent with the expected compositions.

Transport properties

The transport properties of the investigated compounds are shown in Fig. 6. Diligent efforts were directed toward achieving clear and reproducible results. Nonetheless, several difficulties were encountered during the measurements of the electrical transport properties. In addition to the inherent complexities associated with maintaining robust electrical contacts with the elevated temperature range, a substantial tendency of the samples to oxidize was observed. Despite the utilization of a high-purity helium partial pressure atmosphere during measurements, it is plausible that a thin oxide layer may have formed between the measurement probes and the sample surface as temperatures escalated. This occurrence is in line with a recent research work demonstrating the rapid surface oxidation of the related $Yb_{14}MnSb_{11}$ compound around 700 K,[32] and was also pointed out in our recent study on the $Ce_xYb_{4-x}Sb_{2.8}Bi_{0.2}$ solid solution.[22] Although these factors contributed to certain limitations in achieving precise measurements, in particular for the $La_{0.3}Yb_{3.7}Sb_{2.8}Bi_{0.2}$ composition which will not be presented here, the measurements of the binary Yb_4Sb_3 and $La_xYb_{4-x}Sb_{2.8}Bi_{0.2}$ (x = 0.1 and 0.2) compounds were reasonably successful and allowed us to gain valuable insights into the influence of the present dual substitution on the transport properties.

The Seebeck coefficient of all compositions maintains its positive trend above 500 K, consistent with previous studies,

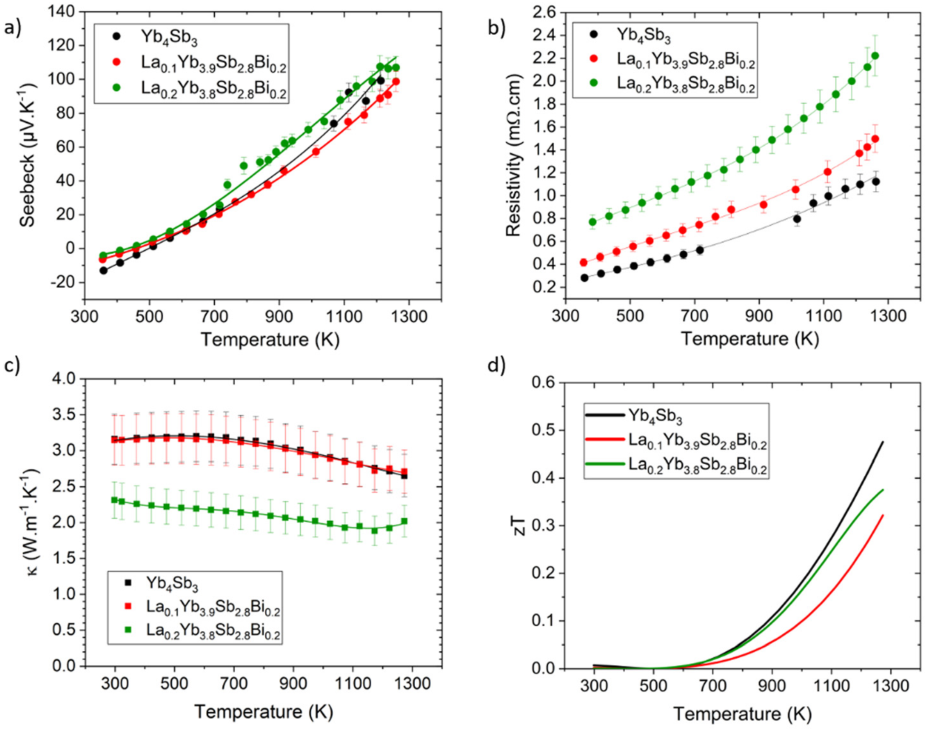

Fig. 6 Thermoelectric properties of Yb_4Sb_3 and $La_xYb_{4-x}Sb_{2.8}Bi_{0.2}$ (x = 0.1 and 0.2) solid solution. (a) Seebeck coefficient, (b) resistivity, (c) thermal conductivity, and (d) figure of merit zT.

indicating a conductive behavior dominated by holes at elevated temperatures. It can be noted that Yb_4Sb_3 presents a higher Seebeck coefficient at 1273 K compared to previous reports (100 μV K^{-1} *versus* 65 μV K^{-1}),[19,20] leading to improved thermoelectric performance. This difference is probably due to the distinct synthesis and shaping routes that might significantly influence the transport properties. Indeed, the co-substitution of Yb by La and Sb by Bi have a relatively modest effect on the Seebeck values. However, a noteworthy enhancement was observed in the case of $La_{0.2}Yb_{3.8}Sb_{2.8}Bi_{0.2}$ with values around 110 μV K^{-1} at 1273 K, possibly stemming from a reduction in hole concentration due to the substantial Yb substitution amount with La atoms (see theoretical section below).

The resistivity trends confirm the characteristic metallic conductive behavior, with values increasing as temperature rises, ranging from 0.3 to 1.1 mΩ cm between 373 and 1273 K for the binary compound Yb_4Sb_3. Substituted compounds exhibit analogous conductive behavior, yet with higher resistivity values compared to the parent Yb_4Sb_3 compound, spanning from 0.8 to 2.2 mΩ cm between 373 and 1273 K for the x = 0.2 composition. This observation is consistent with the anticipated reduction in hole concentration due to La substitution at the Yb site. As the charge carrier concentration could not be measured in this temperature range, this point was assessed *via* theoretical calculations (*vide infra*). That being said, the evolution of the electronic transport properties is similar to that encountered in comparable systems such as $Yb_{21}Mn_4Sb_{18}$ where the substitution of Yb for Na did not change much the Seebeck coefficient while the resistivity was significantly modified.[13]

Thermal conductivities measurements are displayed in Fig. 6c. Yb_4Sb_3 and $La_{0.1}Yb_{3.9}Sb_{2.8}Bi_{0.2}$ exhibit analogous behavior, maintaining a relatively constant value of 3.20 W m^{-1} K^{-1} up to 600 K, followed by a gradual decrease with temperature to 2.65 W m^{-1} K^{-1} at 1273 K for both compounds. The substituted $La_{0.2}Yb_{3.8}Sb_{2.8}Bi_{0.2}$ compound shows lower values, ranging from 2.3 W m^{-1} K^{-1} at lower temperatures down to about 1.9 W m^{-1} K^{-1} at 1173 K. This is in agreement with values already reported for $La_xYb_{4-x}Sb_3$ where thermal conductivities of substituted compounds were decreased by the local mass fluctuation on the Yb site, contributing to enhanced phonon scattering in substituted compounds.[33] While not being pronounced for the $La_{0.1}Yb_{3.9}Sb_{2.8}Bi_{0.2}$ composition, the phenomenon seems accentuated in the $La_{0.2}Yb_{3.8}Sb_{2.8}Bi_{0.2}$ compound, although it doesn't entirely account for the significant reduction in thermal conductivity observed in this particular case. The substantial increase in resistivity also plays an important role according to the Wiedemann–Franz law in diminishing the electronic contribution to thermal conductivity. This might thus explain why the thermal conductivity experiences a notable reduction (about 30%) in the case of the x = 0.2 composition, although this effect seems limited for $La_{0.1}Yb_{3.9}Sb_{2.8}Bi_{0.2}$ as its thermal conductivity was measured to be similar to that of the parent material within a relatively large uncertainty range.

The thermoelectric figure of merit zT of the investigated compounds demonstrates a reasonable performance at elevated temperatures (Fig. 6d). Yb_4Sb_3 achieves a zT value of approximately 0.5 at 1273 K, representing a notable outcome for the pristine compound. The substituted $La_{0.1}Yb_{3.9}Sb_{2.8}Bi_{0.2}$ and

$La_{0.2}Yb_{3.8}Sb_{2.8}Bi_{0.2}$ compounds exhibit zT values of 0.32 and 0.38 at 1273 K, respectively, although slightly lower than that of the pure Yb_4Sb_3 compound. The difference can be attributed primarily to higher resistivities associated with weakly affected Seebeck coefficients in the substituted compounds. The relatively lower thermal conductivity measured for the $x = 0.2$ composition, while not fully compensated with the rise in resistivity, leaves room for further optimization within this family of compounds.

Theoretical insight

The electronic properties of Yb_4Sb_3 were previously theoretically studied using first-principles calculations. V. N. Antonov *et al.* carried out local spin density approximation (LSD) + U DFT calculations to study the heavy fermion Yb_4As_3 compound as well as several isostructural ytterbium pnictides including Yb_4Sb_3.[34] They demonstrated that the width and position of the pnictide p band when going through the pnictogen group of the Periodic Table leads to a transition into a semiconducting behavior towards the light pnictogen element with a charge-transfer gap between the Yb 4f states and the pnictide p band. They also showed that this leads to an increasing carrier concentration and hence an increasing metallic character towards the heavy pnictogen element. M. Shirakawa *et al.* compared their de Haas-van Alphen (dHvA) measurements with local density approximation (LDA) band structure calculations.[35] Further combined experimental and theoretical studies were conducted in order to better understand the dHvA effect in this compound.[36] These studies showed that six bands are involved in the Fermi surfaces. They also computed total and atom-projected density of states (DOS) and showed that the top of the valence band is mainly centered on Yb-4f and Sb-5p levels whereas the bottom of the conduction band is dominated by Yb-5d levels.

We ourselves first performed DFT geometry optimization of the cell parameters and atomic positions of the binary compound Yb_4Sb_3. As often observed in the literature, the volume of the PBE-DFT optimized unit cell is slightly larger (less than 2%) than the one obtained from X-ray diffraction studies (824.8 Å^3 *vs.* 810.1 Å^3). Optimized Yb–Sb bond distances compare very well with the X-ray measured ones: 3.14 Å *vs.* 3.12 Å and 3.36 Å *vs.* 3.32 Å. The spin-polarized band structure of Yb_4Sb_3 is sketched in Fig. 7. It compares quite well with the LDA ones previously reported in the literature. Small differences between up and down band structures suggest weak spin-polarization. This band structure strongly differs from the one reported for the isostructural La_4Sb_3 compound: while the Fermi level crosses the top of the valence band in Yb_4Sb_3, it is located in the bottom of the conduction band in La_4Sb_3.[37] This agrees with the lowest electronic transfer from the metal atoms towards the antimonide network in the case of the ytterbium compound, resulting in a formal Yb(II) oxidation state and p-type character of the compound. This is at the origin of the difference in the transport behavior of Yb_4Sb_3 with regard to other RE_4Sb_3 compounds where RE is a trivalent rare-earth atom.[19] A full theoretical analysis of the electronic structure of both compounds will be further discussed in an upcoming study. The band structure of Yb_4Sb_3 shows that the bands located in the vicinity of the Fermi level are rather flat in the N → P and H → N directions and more dispersive along the Γ → N and P → Γ → H symmetry lines. Such a situation encourages higher Seebeck coefficient as well as good electronic conductivity. Electronic transport properties of the binary were simulated using a semi-classical approach assuming the constant relaxation time approximation. Fig. 8 displays the computed thermopower of Yb_4Sb_3 at 300 and 1300 K as a function of the chemical potential μ. It is noteworthy to mention that the Seebeck coefficient is computed to be negative for $\mu \sim 0$ eV. Even if the band structure suggests that several bands are involved in the conduction, this shows that electrons dominate the conduction at low temperature as observed experimentally. At higher temperature, holes dominate the conduction as expected from the previously published DOS[34] and the band structure sketched in Fig. 7.

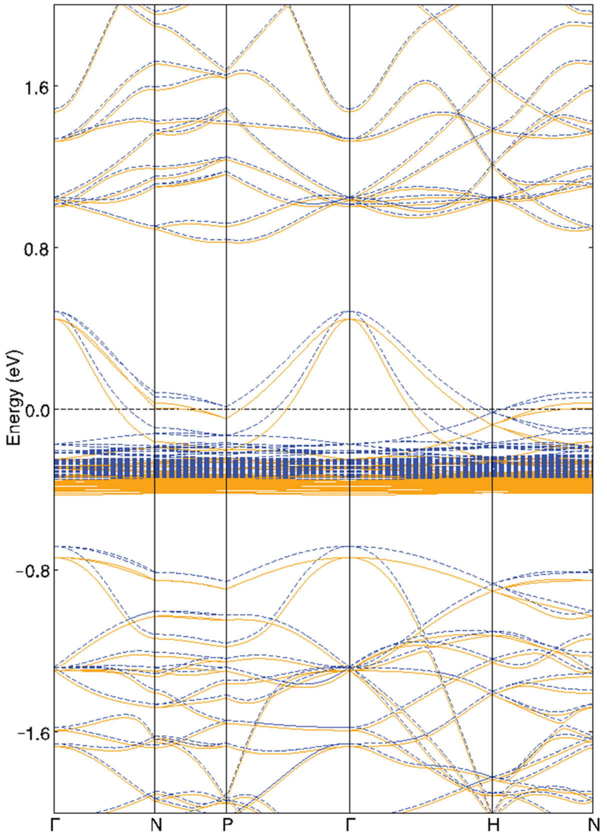

Fig. 7 PBE-DFT spin-up (blue dotted lines) and spin-down (orange solid lines) band structures of Yb_4Sb_3.

As massively exemplified in the literature, the thermopower can be tuned with the variation of the carrier concentration. This can be achieved in particular *via* doping. In order to assess the effect of doping Yb_4Sb_3 with La and Bi, two model compounds were computed: $La_{0.25}Yb_{3.75}Sb_3$ and $Yb_4Sb_{2.75}Bi_{0.25}$. Since Z equals 4 in the crystal structure of the binary compound, the computed models were obtained from the substitution of one Yb atom out of 16 by one La in the case of $La_{0.25}Yb_{3.75}Sb_3$, and of one Sb atom out of 12 by one Bi for

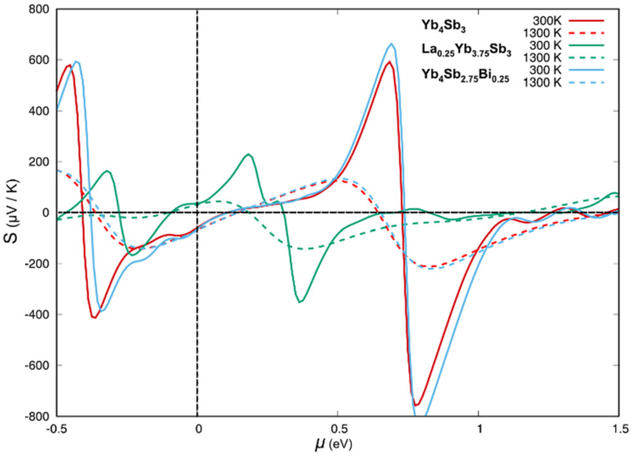

Fig. 8 Seebeck coefficient as a function of the chemical potential μ computed at the PBE-DFT level for Yb_4Sb_3 (red), $La_{0.25}Yb_{3.75}Sb_3$ (green), and $Yb_4Sb_{2.75}Bi_{0.25}$ (blue), at 300 K (solid line) and 1300 K (dashed line).

$Yb_4Sb_{2.75}Bi_{0.25}$. Cell parameters and atomic positions were relaxed without any symmetry constraints. The DFT-optimized volumes of $La_{0.25}Yb_{3.75}Sb_3$ and $Yb_4Sb_{2.75}Bi_{0.25}$ are larger than the optimized one of Yb_4Sb_3 by *ca.* 4%. Such an increase is consistent with the larger size of La and Bi compared to Yb and Sb, respectively.

Total and atom-projected DOS are sketched in Fig. 9. It is obvious that La and Bi substitutions have different impacts on the electronic structure. Bi substitution hardly modifies the electronic structure of Yb_4Sb_3; this is consistent with the isovalent character of both pnictogens. Therefore, assuming similar carrier concentrations, the electronic transport properties of Bi-doped Yb_4Sb_3 are not expected to change significantly as shown in Fig. 8 for the Seebeck coefficient. Indeed, as previously observed experimentally,[21] the Bi-doped Yb_4Sb_3 compound only exhibits a slightly enhanced thermopower irrespective of the chemical potential. On the other hand, the substitution of one Yb(II) atom by one La(III) atom alters much more the electronic structure and the computed electronic transport properties. One can note that spin polarization decreases in the La-doped model compound whereas it hardly changes in the Bi-doped model compound. The additional electrons brought by the lanthanum atoms contribute to fill the valence band in $La_{0.25}Yb_{3.75}Sb_3$, making the compound less electron conductive. This also favours a p-type conduction and explains why the Seebeck coefficient turns positive at the Fermi level at both simulated temperatures. The thermopower is computed lower than that of the parent compound, regardless of the chemical potential. Assuming a rigid band model, the extra electron provided by La implies an increase in the Fermi level that crosses mainly dispersive bands in the Γ → N and P → Γ → H directions (see Fig. 7), which is consistent with a Seebeck coefficient reduction.

Conclusions

This study delved into and discussed the potential thermoelectric applications of Yb_4Sb_3 and related substituted compounds up to 1300 K. By simultaneously substituting Yb with La and Sb with Bi, we aimed to enhance their performance through the optimization of their figure of merit zT. Exploration of the solubility limit of the $La_xYb_{4-x}Sb_{2.8}Bi_{0.2}$ solid solution revealed a maximum value of $x = 0.3$, beyond which complete substitutions were not obtained. Subsequent syntheses of Yb_4Sb_3 and $La_xYb_{4-x}Sb_{2.8}Bi_{0.2}$

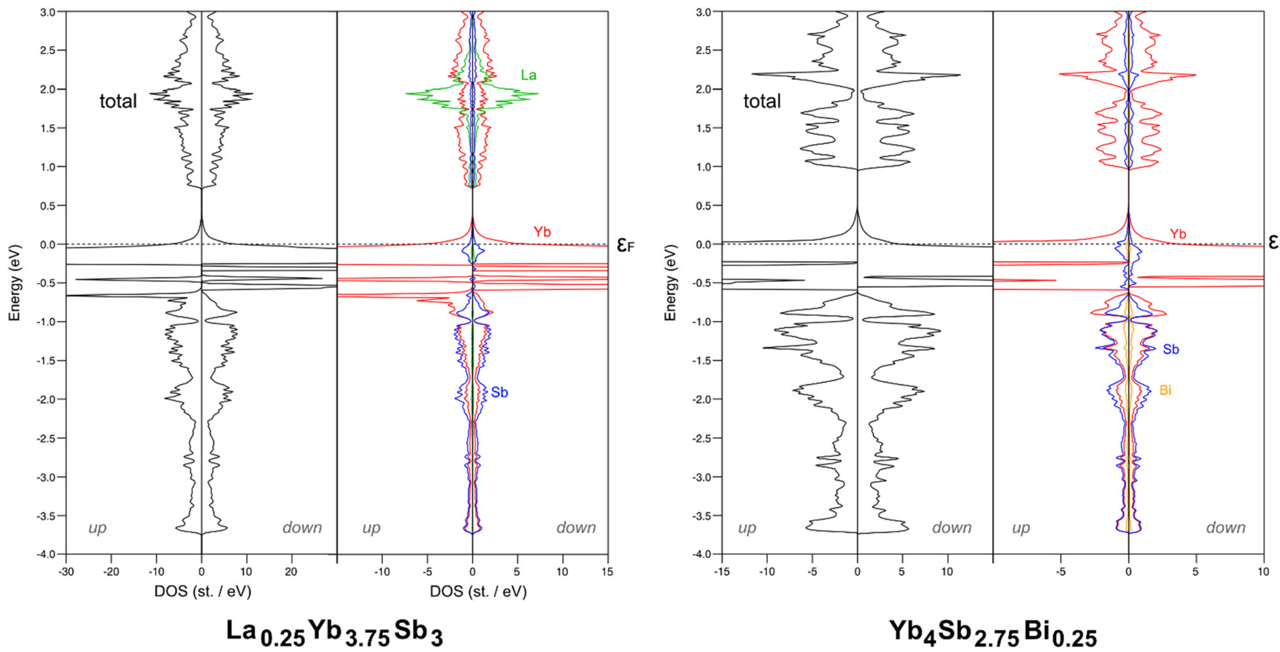

Fig. 9 PBE-DFT total and atom projected DOS computed for $La_{0.25}Yb_{3.75}Sb_3$ (left) and $Yb_4Sb_{2.75}Bi_{0.25}$ (right).

(x = 0.1, 0.2 and 0.3) on a larger scale followed by high-temperature transport properties measurements brought substantial new insights. As expected for materials exhibiting metallic conductive behavior, resistivity showcases a temperature-dependent increase while remaining in a desirable range. The Seebeck coefficients were hardly affected by the co-substitution with values reaching 110 $\mu V\ K^{-1}$ at 1273 K for x = 0.2. First-principles calculations helped in understanding the electronic transport properties of Yb_4Sb_3, especially the n-type to p-type transition at high temperature. These calculations also confirmed that Bi-substitution left electronic transport properties unaffected, while La substitution did not enhance the Seebeck coefficient but rather increased resistivity. Furthermore, this investigation unveiled a promising zT of 0.5 for Yb_4Sb_3 at 1300 K, which is the highest maximum zT value reported so far for the parent compound, confirming its thermoelectric potential in high-temperature scenarios. While both experimental and theoretical results have shown that the dual substitutions did not yield a substantial enhancement of zT for the $La_xYb_{4-x}Sb_{2.8}Bi_{0.2}$ (x = 0.1 and 0.2) solid solution, the study lays a foundation for further optimization. Future directions should involve the exploration of alternative substitutions, innovative nano-structuring, or defect engineering to potentially achieve elevated zT values.

Author contributions

H. Bouteiller: conceptualization, data curation, formal analysis, investigation, methodology, validation, visualization, writing – original draft, writing – review & editing. V. Pelletier: software, data curation, formal analysis, investigation, validation, visualization, writing – review & editing. S. Le Tonquesse: conceptualization, data curation, formal analysis, investigation, validation, visualization, writing – review & editing. B. Fontaine: software, data curation, formal analysis, investigation, supervision. T. Mori: funding acquisition, resources, supervision, writing – review & editing. J.-F. Halet: formal analysis, investigation, software, supervision, project administration, writing – review & editing. R. Gautier: conceptualization, data curation, formal analysis, investigation, methodology, software, supervision, validation, visualization, project administration, writing – review & editing. D. Berthebaud: conceptualization, formal analysis, investigation, methodology, project administration, resources, supervision, writing – review & editing. F. Gascoin: conceptualization, formal analysis, funding acquisition, investigation, methodology, project administration, resources, supervision, writing – review & editing.

Conflicts of interest

There are no conflicts to declare.

Acknowledgements

The authors are grateful to the Agence Nationale de la Recherche (ANR – Project HIGHTHERM – Ref ANR-18-CE05-0037) and the Japan Society for the Promotion of Science (JSPS – PE21708) for financial support. Support from JST Mirai Program JPMJMI19A1 is also acknowledged.

Notes and references

1 D. Beretta, N. Neophytou, J. M. Hodges, M. G. Kanatzidis, D. Narducci, M. Martin- Gonzalez, M. Beekman, B. Balke, G. Cerretti, W. Tremel, A. Zevalkink, A. I. Hofmann, C. Müller, B. Dörling, M. Campoy-Quiles and M. Caironi, *Mater. Sci. Eng. R Rep.*, 2019, **138**, 100501.
2 J. Mao, Z. Liu, J. Zhou, H. Zhu, Q. Zhang, G. Chen and Z. Ren, *Adv. Phys.*, 2018, **67**, 69–147.
3 G. J. Snyder and E. S. Toberer, *Nat. Mater.*, 2008, **7**, 105–114.
4 T. Mori, *JOM*, 2016, **68**, 2673–2679.
5 R. Freer and A. V. Powell, *J. Mater. Chem. C*, 2020, **8**, 441.
6 A. P. Gonçalves and C. Godart, *Eur. Phys. J. B*, 2014, **87**, 1–29.
7 S. Hébert, D. Berthebaud, R. Daou, Y. Bréard, D. Pelloquin, E. Guilmeau, F. Gascoin, O. Lebedev and A. Maignan, *J. Phys.: Condens. Matter*, 2015, **28**, 013001.
8 M. Wolf, R. Hinterding and A. Feldhoff, *Entropy*, 2019, **21**, 1058.
9 T. Mori, *J. Solid State Chem.*, 2019, **275**, 70–82.
10 B. Cook, *Energies*, 2022, **15**, 2957.
11 V. Ravi, S. Firdosy, T. Caillat, E. Brandon, K. Van Der Walde, L. Maricic and A. Sayir, *J. Electron. Mater.*, 2009, **38**, 1433–1442.
12 S. R. Brown, S. M. Kauzlarich, F. Gascoin and G. Jeffrey Snyder, *Chem. Mater.*, 2006, **18**, 1873–1877.
13 A. He, S. K. Bux, Y. Hu, D. Uhl, L. Li, D. Donadio and S. M. Kauzlarich, *Chem. Mater.*, 2019, **31**, 8076–8086.
14 J. W. G. Bos, in *Thermoelectric Energy Conversion*, ed. R. Funahashi, Woodhead Publishing, 2021, pp. 125–142.
15 Z. Ren, Y. Lan and Q. Zhang, *Advanced thermoelectrics: materials, contacts, devices, and systems*, 2018.
16 G. J. Snyder and A. H. Snyder, *Energy Environ. Sci.*, 2017, **10**, 2280–2283.
17 A. F. May, J. P. Fleurial and G. J. Snyder, *Chem. Mater.*, 2010, **22**, 2995–2999.
18 D. Hohnke and E. Parthé, *Acta Crystallogr.*, 1966, **21**, 435–437.
19 A. Chamoire, F. Gascoin, C. Estournès, T. Caillat and J. C. Tédenac, *Dalton Trans.*, 2010, **39**, 1118–1123.
20 A. Chamoire, R. Viennois, J. C. Tedenac, M. M. Koza and F. Gascoin, *J. Electron. Mater.*, 2011, **40**, 1171–1175.
21 A. Chamoire, PhD thesis, Université de Montpellier, 2009.
22 S. Le Tonquesse, H. Bouteiller, Y. Matsushita, A. Cortez, S. K. Bux, K. Imasato, M. Ohta, J.-F. Halet, T. Mori, F. Gascoin and D. Berthebaud, *ACS Appl. Energy Mater.*, 2023, **6**(19), 10088–10097.
23 J. Rodriguez-Carvajal, Abstr. Satell. Meet. Powder Diffr. XV Congr. IUCr, 1990, 127.
24 G. Kresse and J. Hafner, *Phys. Rev. B: Condens. Matter Mater. Phys.*, 1993, **47**, 558.
25 G. Kresse and J. Furthmüller, *Phys. Rev. B: Condens. Matter Mater. Phys.*, 1996, **54**, 11169.

26 G. Kresse and J. Furthmüller, *Comput. Mater. Sci.*, 1996, **6**, 15–50.

27 J. P. Perdew, K. Burke and M. Ernzerhof, *Phys. Rev. Lett.*, 1996, **77**, 3865–3868.

28 H. J. Monkhorst and J. D. Pack, *Phys. Rev. B: Solid State*, 1976, **13**, 5188–5192.

29 T. J. Scheidemantel, C. Ambrosch-Draxl, T. Thonhauser, J. V. Badding and J. O. Sofo, *Phys. Rev. B: Condens. Matter Mater. Phys.*, 2003, **68**, 125210.

30 G. K. H. Madsen, *J. Am. Chem. Soc.*, 2006, **128**, 12140–12146.

31 G. K. H. Madsen, J. Carrete and M. J. Verstraete, *Comput. Phys. Commun.*, 2018, **231**, 140–145.

32 A. P. Justl and S. M. Kauzlarich, *ACS Appl. Mater. Interfaces*, 2022, **14**, 47246–47254.

33 E. S. Toberer, L. L. Baranowski and C. Dames, *Annu. Rev. Mater. Res.*, 2012, **42**, 179–209.

34 V. N. Antonov, A. N. Yaresko, A. Y. Perlov, P. Thalmeier, P. Fulde, P. M. Oppeneer and H. Eschrig, *Phys. Rev. B: Condens. Matter Mater. Phys.*, 1998, **58**, 9752–9762.

35 M. Shirakawa, M. Ona, H. Aoki and A. Ochiai, *Acta Phys. Pol., B*, 2003, **34**, 1157.

36 M. Kakihana, K. Nishimura, Y. Ashitomi, T. Yara, D. Aoki, A. Nakamura, F. Honda, M. Nakashima, Y. Amako, Y. Uwatoko, T. Sakakibara, S. Nakamura, T. Takeuchi, Y. Haga, E. Yamamoto, M. Hedo, T. Nakama and Y. Ōnuki, *J. Electron. Mater.*, 2017, **46**, 3572–3584.

37 K. Takegahara, H. Harima and T. Kasuya, *J. Magn. Magn. Mater.*, 1985, **52**, 307–309.